Cement and Concrete Research 90 (2016) 80–88

Contents lists available at ScienceDirect

Cement and Concrete Research

journal homepage: www.elsevier.com/locate/cemconres

Edge dislocations in dicalcium silicates: Experimental observations and atomistic analysis

Rouzbeh Shahsavari [a,b,c,*], Lu Chen [a], Lei Tao [a]

[a] Department of Civil and Environmental Engineering, Rice University, Houston, TX 77005, United States
[b] Department of Material Science and NanoEngineering, Rice University, Houston, TX 77005, United States
[c] Smalley Institute for Nanoscale Science and Technology, Rice University, Houston, TX, 77005, United States

ARTICLE INFO

Article history:
Received 29 October 2015
Received in revised form 7 September 2016
Accepted 14 September 2016
Available online 28 September 2016

Keywords:
Dicalcium silicates (Ca_2SiO_4)
Atomistic simulation
Edge dislocation
Crystal defects
Dislocation-mediated properties

ABSTRACT

Understanding defects and influence of dislocations on dicalcium silicates (Ca_2SiO_4) is a challenge in cement science. We report a high-resolution transmission electron microscopy image of edge dislocations in Ca_2SiO_4, followed by developing a deep atomic understanding of the edge dislocation-mediated properties of five Ca_2SiO_4 polymorphs. By decoding the interplay between core dislocation energies, core structures, and nucleation rate of reactivity, we find that γ-C2S and α-C2S polymorphs are the most favorable polymorphs for dislocations in Ca_2SiO_4, mainly due to their large pore channels which take away majority of the distortions imposed by edge dislocations. Furthermore, in the context of edge dislocation, while α-C2S represents the most active polymorph for reactivity and crystal growth, β-C2S represents the most brittle polymorph suitable for grinding. This work is the first report on the atomistic-scale analysis of edge dislocation-mediated properties of Ca_2SiO_4 and may open up new opportunities for tuning fracture and reactivity processes of Ca_2SiO_4 and other cement components.

1. Introduction

Defects such as stacking faults and dislocations, which form and propagate in crystals, significantly impact many chemical and physical properties of materials. For example, material plasticity and crack propagation are markedly influenced by dislocation core structure, dislocation-dislocation interactions, and dislocation mobilities [1]. Similarly, crystal growth can be affected by both screw [2] and edge screw dislocations [3–4]. Although dislocations have been extensively studied in metals [5–8] semiconductors [9–13] and some simple ceramics, [14–21] there have been few attempts in characterizing such defects in more complex compounds such as zeolites, forsterite (Mg_2SiO_4) and dicalcium silicates (Ca_2SiO_4) [22]. The difficulty arises due to the complicated formatting components, heterogeneous nature, and the packing arrangements of several atomic species, which often lead to low symmetry crystals.

Several experimental techniques are used to study dislocations including surface and decoration methods, field ion microscopy, X-ray diffraction, high resolution transmission electron microscopy (HRTEM) and Z-contrast imaging techniques [1,23–25]. While these experiments provide means to observe and infer information about the dislocation structure, distribution and arrangement, they cannot provide precise information on dislocation energetics and mobilities, which often control the dislocations slip, slip-planes and other dislocation-mediated phenomena such as macro scale ductility and crystal growth. From a modeling standpoint, although semi-continuum Peierls-Nabarro models [26–27] are widely used to study dislocations by introducing the energies of generalized stacking faults from density functional theory to continuum model of the dislocations, the significant constraint of planar dislocations limits their applicability [28]. Alternative approaches use atomic scale simulations to calculate explicitly the dislocation core structure. In this group, fully periodic dipole approaches can simulate an infinite array of dislocations (e.g. line defects in silicon [10–11], extended defects in diamond cubic crystals [29], and impurities at edge dislocations [9]). However, this method is less straightforward for complex crystals, due to the correction for interactions between dislocation core fields [30–31], and contributions from core traction in the dislocation formation energy [32]. Recently developed cluster embedded models [33–34], based on one-dimensional periodic boundary conditions, allow to investigate systematically an isolated dislocation with atomic-scale fidelity. The cluster model, employed in this work, has been already highly successful in predicting the core energy and structure of dislocations in different material classes including ionic materials (MgO) [34], zeolites [35], wadsleyite minerals (β-Mg_2SiO_4) [36] and paracetamol (OH-$C_6H_4NHCOCH_3$), a widely used drug known as acetaminophuse [34].

The objective of the present work is to study edge dislocations in structurally complex and low symmetry oxides, which are of both

* Corresponding author at: Department of Civil and Environmental Engineering, Rice University, Houston, TX 77005, United States.
E-mail address: rouzbeh@rice.edu (R. Shahsavari).

http://dx.doi.org/10.1016/j.cemconres.2016.09.012
0008-8846/

scientific and technological importance. As a model system, we focus on five reversible polymorphs of dicalcium silicates (Ca_2SiO_4), key ingredients of industrial cement clinkers where the defect characteristics and integrity of Ca_2SiO_4 crystals' structures play a key role in clinker grinding processes as well as crystal growth mechanisms [37]. The latter is of particular significance in hydration of Ca_2SiO_4 to precipitate semi-crystalline, non-stoichiometric calcium-silicate-hydrate (C-S-H) phase, which is the chief source of strength and durability in cementitious materials [37–38]. Compared to tricalcium silicate (Ca_3SiO_5), the more energy-intensive and dominant ingredient of the cement clinker, Ca_2SiO_4 (also known as belite with shortened notation of C2S in cement chemistry) needs at least ~100 °C lower temperature to produce. However, it requires more energy for grinding it and reacts slower with water, thereby leading to delayed strength development in cement paste [39]. But given the overall economical gain due to lower manufacturing temperature of Ca_2SiO_4 and the augmented need to reduce greenhouse gas emissions from cement plants (currently cement manufacturing is responsible for 5–10% of the worldwide anthropogenic CO_2 emissions), there is an urgent necessity to tune grinding properties and reactivity of Ca_2SiO_4 to make it a more sustainable cement clinker. In this perspective, understanding the defects and edge dislocations in Ca_2SiO_4 can provide important information on how to modulate and promote the salient properties of Ca_2SiO_4.

Ca_2SiO_4 has a crystalline structure that is composed of SiO_4^{4-} tetrahedra and Ca^{2+} ions with a sequence of five reversible polymorphs, namely α, α_H, α_L, β and γ, from high to low temperatures (Fig. 1). X-ray analysis [40] have provided the exact crystal and atomic structure of these polymorphs, which can be transformed from one to another via changing the crystal symmetry, disorder of SiO_4^{4-} groups and slight changes in the position of the Ca^{2+} atoms [41–44]. The α and β polymorphs have monoclinic crystals while α_H, $\alpha_L$and γ polymorphs have orthorhombic crystals [37] (Fig. 2).

Dislocations in Ca_2SiO_4 arise from the growth and cooling processes during cement manufacturing, and presence of impurities [45–47]. Different crystal faces will behave differently during dissolution, etch pit formation, and hydration, depending on the size of the Burgers vector *b* as well as type and density of dislocations [45]. In view of the complexity of low-symmetry cement crystals, very limited experiments are reported so far on the observation of dislocations [47–51], and initiation of etch-pit formation from dislocations [37,52]. In this report, we focus on filling this knowledge gap by providing a clear HRTEM image of formation of edge dislocations in belite, followed by developing a deep atomic-based understanding of the dislocation-mediated properties of Ca_2SiO_4 polymorphs, thus providing de novo insights and strategies for bottom-up engineering of cement clinkers.

2. Methods

2.1. Materials and characterization

Pristine dicalcium silicate (99% purity) was purchased from Sarl Mineral Research Processing Company in France and used as is for characterization. Transmission electron microscopy (TEM) and HRTEM experiments were performed by depositing a small belite sample onto a carbon-coated copper grid. Since the dicalcium silicate was in the powder form, not focused ion beam (FIB) milling was required. The sample was analyzed using a JEOL 2100 Field Emission Gun Transmission Electron Microscope at several different locations until a clear edge dislocation was observed.

2.2. Cluster embedded atom model

For our computational study, we adopted a simulation strategy, so-called cluster embedded atom model, to combine an atomic scale dislocation core with a description of the extended crystal based on continuum linear elasticity [33]. This method takes advantage of the symmetry of Volterra dislocation to create a model using periodic boundary conditions along the dislocation line while only involving a finite cluster of atoms perpendicular to the dislocation line. A convention in this paper is to lay the edge dislocation line along the z axis and its Burgers vector along the x direction. The magnitude of the dislocation is equal to one lattice distance.

We used a three stage approach to create the models of the edge dislocation. The first stage is constructing a charge neutral disk-shape supercell containing the defect–free crystal structure in which the one-dimensional periodicity passes through the central axis of the disk (z axis). The radius of the simulation cell is 90 Å to accommodate relaxation around the core. Typical number of atoms in each simulation cell of the dicalcium silicate is ~15,000–17,000. Charge neutrality of the simulation cells is satisfied by breaking the small extra charge (as the result of cutting a cylinder from the supercell) to all the ~15,000 atoms, hence leading to less than 1% change in the partial charge of each individual atom. We assume this minimal change in partial charges would not affect the accuracy of the force field predictions.

The second stage involves introducing the edge dislocation based on anisotropic linear elasticity [53]. Fig. 3a shows the conceptual model of introducing an edge dislocation in a homogenous linear elastic body, which involved three basic steps: i) identification of the origin of the dislocation, which is a vacant point between the atoms. Note that in continuum (not atomistic) systems, a small part in the center is removed to eliminate the singularity of the original point based on elastic theory. However, this issue is not a concern in our atomic simulation cells since a vacant point between the atoms serves as the origin, ii) a solid line from the perimeter to the center of the cylinder is drawn to represent the "cut". The direction of this "cut", which is along the shortest lattice dimension determines the x axis used in the mathematical formula of anisotropic elasticity, and iii) atoms at opposite sides of the "cut" are displaced horizontally by a Burgers vector to form an edge dislocation.

The dislocated structure of the simulation cell in Fig. 3a is constructed in practice by the elastic displacement field, mapping the location of atoms in the bulk cell to the equivalent point in the dislocated cell. The elastic displacement field is only a function of Burgers vector, atomic positions and elastic properties of the crystals. For the orthorhombic crystals considered in this work, the displacement field is entirely in the plane of Burgers vector ($u_z = 0$) and is given by following equations [53]. If $\lambda^4 < \Lambda^2$, the displacement field corresponding to the *x* component of the Burgers vector reads

$$u_x = \frac{b_x}{4\pi}\left[\arctan\left\{\frac{\sqrt{2\left(\lambda^2-\Lambda\right)}\tan\theta}{1-\lambda^2\tan^2\theta}\right\} - \frac{\Lambda + S_{12}/S_{11}}{\sqrt{\Lambda^2-\lambda^4}}\arctan\left\{\frac{\sqrt{-2\left(-\lambda^2+\Lambda\right)}\tan\theta}{1+\lambda^2\tan^2\theta}\right\}\right] \quad (1)$$

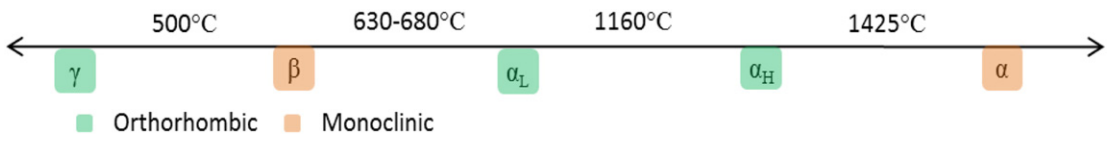

Fig. 1. Five thermodynamically reversible Ca_2SiO_4 polymorphs. The Greek L and H subscripts denote high temperature and low temperature variants.

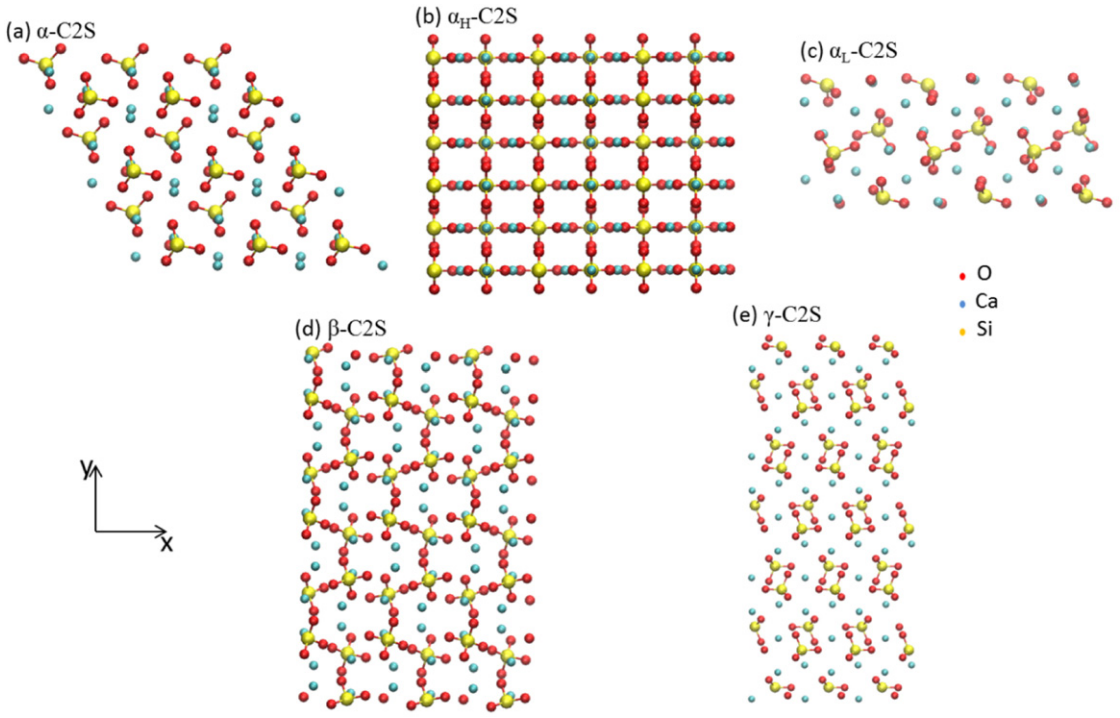

Fig. 2. Atomic snapshots of dicalcium silicate polymorphs: (a) α-C2S (b) α_H-C2S (c) α_L-C2S (d) β-C2S (e) γ-C2S.

$$u_y = \frac{b_x}{4\pi}\left[-\frac{\left(\lambda^2 + S_{12}/S_{11}\right)}{\sqrt{2\left(\lambda^2-\Lambda\right)}}\ln r^2\sqrt{\cos^4\theta+\lambda^4\sin^4\theta-\frac{1}{2}\Lambda\sin^2 2\theta} + \frac{\left(\lambda^2-S_{12}/S_{11}\right)}{2\sqrt{-2\left(\lambda^2+\Lambda\right)}}\ln\left\{\frac{\cos^2\theta-\left(\Lambda-\sqrt{\Lambda^2-\lambda^4}\right)\sin^2\theta}{\cos^2\theta-\left(\Lambda+\sqrt{\Lambda^2-\lambda^4}\right)\sin^2\theta}\right\}\right] \quad (2)$$

while that of the *y* component of the Burgers vector reads

$$u_x = \frac{b_y}{4\pi\lambda^2}\left[\frac{\left(\lambda^2 + S_{12}/S_{11}\right)}{\sqrt{2\left(\lambda^2-\Lambda\right)}}\ln r^2\sqrt{\cos^4\theta+\lambda^4\sin^4\theta-\frac{1}{2}\Lambda\sin^2 2\theta} + \frac{\left(\lambda^2-S_{12}/S_{11}\right)}{2\sqrt{-2\left(\lambda^2+\Lambda\right)}}\ln\left\{\frac{\cos^2\theta-\left(\Lambda-\sqrt{\Lambda^2-\lambda^4}\right)\sin^2\theta}{\cos^2\theta-\left(\Lambda+\sqrt{\Lambda^2-\lambda^4}\right)\sin^2\theta}\right\}\right] \quad (3)$$

$$u_y = \frac{b_y}{4\pi}\left[\arctan\left\{\frac{\sqrt{2\left(\lambda^2-\Lambda\right)}\tan\theta}{1-\lambda^2\tan^2\theta}\right\} + \frac{\Lambda+S_{12}/S_{11})}{\sqrt{\Lambda^2-\lambda^4}}\arctan\left\{\frac{\sqrt{-2\left(\lambda^2+\Lambda\right)}\tan\theta}{1+\lambda^2\tan^2\theta}\right\}\right] \quad (4)$$

In above, $\lambda^4 = \frac{S_{22}}{S_{11}}$; $\Lambda = -\frac{2S_{12}+S_{66}}{2S_{11}}$; u_x, u_y, and u_z are atomic displacements due to the elastic theory; *x*, *y*, and *z* are the Cartesian atomic positions in the bulk cell, S_{ij} are the components of the elastic compliance tensor, and $\theta = \tan^{-1}(\frac{x}{y})$. Similarly, if $\lambda^4 > \Lambda^2$ for the *x* component of the Burgers vector we have

$$u_x = \frac{b_x}{4\pi}\left[\arctan\left\{\frac{\sqrt{2\left(\lambda^2-\Lambda\right)}\tan\theta}{1-\lambda^2\tan^2\theta}\right\} + \frac{(\Lambda+S_{12}/S_{11})}{\sqrt{\left(\lambda^4-\Lambda^2\right)}}\ln\left\{\frac{\cos^2\theta+\lambda^2\sin^2\theta-\sqrt{\frac{\Lambda+\lambda^2}{2}}\sin^2\theta}{\cos^2\theta+\lambda^2\sin^2\theta+\sqrt{\frac{\Lambda+\lambda^2}{2}}\sin^2\theta}\right\}\right] \quad (5)$$

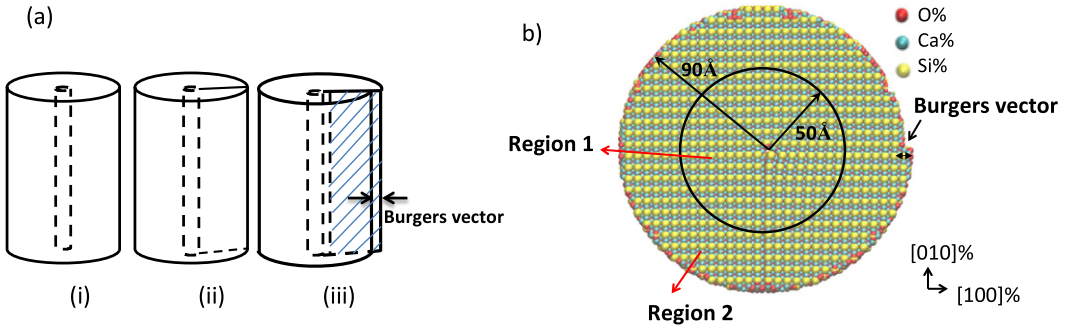

Fig. 3. (a) A conceptual model of introducing edge dislocation based on linear elasticity. (b) A typical atomic illustration of the edge dislocation in dicalcium silicate. The atoms in the region 2 are fixed during the energy minimization.

$$u_y = \frac{b_x}{4\pi}\left[-\frac{\left(\lambda^2 + S_{12}/S_{11}\right)}{\sqrt{2\left(\lambda^2 - \Lambda\right)}} \ln r^2 \sqrt{\cos^4\theta + \lambda^4 \sin^4\theta - \frac{1}{2}\Lambda \sin^2 2\theta} + \frac{\left(\lambda^2 - S_{12}/S_{11}\right)}{\sqrt{2\left(\lambda^2 + \Lambda\right)}} \arctan\left\{ \frac{\sqrt{\lambda^4 - \Lambda^2}}{\cot^2\theta - \Lambda} \right\} \right] \quad (6)$$

while the y component of the Burgers vector gives:

$$u_x = \frac{b_y}{4\pi\lambda^2}\left[-\frac{\left(\lambda^2 + S_{12}/S_{11}\right)}{\sqrt{2\left(\lambda^2 - \Lambda\right)}} \ln r^2 \sqrt{\cos^4\theta + \lambda^4 \sin^4\theta - \frac{1}{2}\Lambda \sin^2 2\theta} + \frac{\left(\lambda^2 - S_{12}/S_{11}\right)}{\sqrt{2\left(\lambda^2 + \Lambda\right)}} \arctan\left\{ \frac{\lambda^4 - \Lambda^2}{\cot^2\theta - \Lambda} \right\} \right] \quad (7)$$

$$u_y = \frac{b_y}{4\pi}\left[\arctan\left\{ \frac{\sqrt{2\left(\lambda^2 - \Lambda\right)}\tan\theta}{1 - \lambda^2 \tan\theta} \right\} + \frac{(\Lambda + S_{12}/S_{11})}{\sqrt{\left(\lambda^4 - \Lambda^2\right)}} \ln\left\{ \frac{\cos^2\theta + \lambda^2 \sin^2\theta - \sqrt{\frac{\Lambda + \lambda^2}{2}}\sin 2\theta}{\cos^2\theta + \lambda^2 \sin^2\theta + \sqrt{\frac{\Lambda + \lambda^2}{2}}\sin 2\theta} \right\} \right] \quad (8)$$

For the monoclinic crystals, i.e. β-C2S and α-C2S, we still apply the above solution. The underlying assumption is that the energy relaxation carried out during atomistic simulations (to be discussed shortly) can compensate the insufficient accuracy of the orthotropic solution for monoclinic crystals. Indeed, the extra elastic constants of monoclinic versus orthotropic crystals influence mainly the angle between the actual slip plane and the Burgers vector. However, in view of the fact that the slip plane in edge dislocation is along the most close-packed plane [1], the slip plane could be determined beforehand (step ii in above), and the Burgers vector can be set as the lattice distance along that direction. Therefore, although the above elastic formula are obtained for orthorhombic crystals, with reasonable orientation of the slip plane, the atomic structure far away from the dislocation core should be accurate even in monoclinic structures deformed by a perfect edge dislocation.

The final step needed to generate a model of the dislocation core is to let the atoms move to find a low energy configuration. While the linear elastic displacement field is accurate for the atoms far away from the core, the energy minimization corrects for the non-linear elasticity close to the core. This combination allows the possibility of inhomogeneous strains, accounts for the atomic scale structure of the core and allows the reconstruction if the core causes deformation of the surrounding crystal [33]. All energy minimizations in this work were performed using conjugate gradient algorithm as implemented in the GULP code [54]. To simulate the existence of the extended crystal, a 40 Å outer rim of the atoms were held fixed in the configuration predicted by the linear elasticity (region 2 in Fig. 3b). Atoms within the 50 Å of the center of the cell were allowed to relax (region 1). The choice of the thickness of the region 2 (40 Å tim), which is larger than the real space of the Coulomb cutoff radius ensures that the mobile atoms do not interact with the edge of the atomistic model.

To describe the interatomic interactions of Ca2SiO4 crystals, we employed ClayFF potential [55]. This force field is based on an ionic–covalent description of metal–oxygen interactions and has been highly successful in predicting several structural and mechanical properties of crystalline minerals [56–57]. In ClayFF, metal–oxygen interactions are based on a 12–6 Lennard-Jones potential combined with Coulombic interactions. The empirical parameters and partial atomic charges are obtained from cluster and periodic density functional theory, quantum chemical calculations of simple oxide, hydroxide, and oxyhydroxide model compounds with well-defined structures. To our knowledge, ClayFF potential is currently the best potential to describe the structural and elastic properties of cement clinkers (see supporting information). Using this force field, the extraction of the elastic constants and Young moduli from atomistic simulations is straightforward by calling the property calculation option in GULP. For instance, elastic constants are obtained by taking the second derivative of energy density with respect to strains. The detailed parameters of ClayFF potential is given in Tables S1–2, and the comparison of its predictions with experiments for lattice parameters and elastic constants of C2S polymorphs are given in Tables S3–S4. The elastic properties of C2S are shown in Table 1.

Reuss-Voigt-Hill method is used in Table 1 to obtain the average shear and bulk moduli. The average Young modulus is the arithmetic average of the Young moduli along the X, Y and Z direction for each crystal. Regarding the comparison of the mechanical properties of ClayFF prediction with experiments, we could not find specific data for elastic constants or average mechanical properties of the C2S polymorphs in the literature. However, there is a reported Young modulus of 130 GPa for C2S with ±20 standard deviation. This value matches well with our predicted elastic moduli (~112–113 GPa). However, we stress that in the aforementioned experimental study, their C2S is a mixture of all polymorphs (they could not isolate a specific polymorph) with unknown percentages of the constituents. Furthermore, this experimental C2S has stabilizing elements and impurities that are common in industrial C2S samples. Thus, more accurate comparison can be done in the future when more specific data become available experimentally.

2.3. Calculation of dislocation formation energy and dislocation core radius

Once an energy minimum has been achieved, various techniques as described below are used to probe the structural and energetic characteristics of the dislocation core. An important information is a measure of the thermodynamic stability of the dislocation - the dislocation formation energy - which is defined as the work per unit length required to introduce a dislocation to a bulk material. The distortion induced by dislocation makes the total dislocation formation energy a combination of two parts: the energy of the dislocation core and the elastic energy of the extended crystal system as a result of the dislocation core. In

Table 1
Calculated average elastic properties of C2S polymorphs.

	α-C2S	α_H-C2S	α_L-C2S	β-C2S	γ-C2S
K_V (GPa)	60.32	70.94	70.99	49.83	57.80
K_R (GPa)	59.00	62.39	67.37	43.96	56.13
K_{VRH} (GPa)	59.66	66.67	69.18	46.89	56.97
G_V (GPa)	32.20	34.75	34.26	23.99	30.14
G_R (GPa)	30.14	23.83	30.55	18.46	28.39
G (GPa)	31.17	29.29	32.41	21.22	29.27
E_x (GPa)	75.19	140.94	153.22	68.55	70.97
E_y (GPa)	67.61	93.88	97.41	36.30	50.68
E_z (GPa)	76.28	101.19	88.74	31.25	73.76
E (GPa)	73.02	112.00	113.12	45.37	65.14
E^* (GPa)	130 ± 20				

K_V: bulk modulus Voigt average (upper bound on K).
K_R: bulk modulus Reuss average (lower bound on K).
K_{VRH}: bulk modulus VRH average, $2K_{VRH} = K_V + K_R$.
G_V: bulk modulus Voigt average (upper bound on G).
G_R: bulk modulus Reuss average (lower bound on G).
G_{VRH}: shear modulus VRH average, $2G_{VRH} = G_V + G_R$.
E_x: Young modulus along X directions.
E_y: Young modulus along Y directions.
E_z: Young modulus along Z directions.
E: average Young's modulus, i.e. arithmetic average of Young modulus along X, Y and Z directions.
E^*: experimental reported Young's modulus of C2S.

contrast to the point or planar defects, there is no unique dislocation formation energy per unit length of dislocation. The formation energy includes an elastic part arising from elastic strain distributed across the extended crystal and thus is a function of the size of the crystal from the dislocation line. The total formation energy, E, stored within a cylindrical crystal of radius r is given by [53]

$$E(r) = E_{core} + \frac{Xb^2}{4\pi(1-\nu)} Ln\left(\frac{r}{r_0}\right) \quad (9)$$

where r_0 is the size of the dislocation core with energy E_{core}, b is the length of the Burgers vector as before, and X is an energy factor depending on the symmetry of the elastic constant tensor, and equal to shear modulus in isotropic materials.

There are two unknowns in Eq. (9), i.e. E_{core} and r_0, which can be determined by calculating $E(r)$ for various radii. To do so, the cell derived from the energy minimization is divided into two regions. Region 1 contains the atoms found inside a certain radius, r, and region 2 is the rest of atoms outside of the region 1 (conceptually similar to regions shown in Fig. 3b). Then, the energy of the simulation cell containing the dislocation is partitioned into three parts: i) interactions between atoms within region 1, E_d^{11}, ii) interactions between atoms in region 2, E_d^{22}, and iii) interactions between the two regions, E_d^{12} or E_d^{21}. Equivalently, the energies in the perfect crystal can be partitioned in the same way as E_p^{11}, E_p^{12} (or E_p^{21}) and E_p^{22}. Then, the dislocation formation energy stored within region 1 is given by [22]

$$E(r) = \left[E_d^{11} + E_d^{12}\right] - \left[E_p^{11} + E_p^{12}\right] \quad (10)$$

where $E(r)$ is calculated for various radii and the resulting data is fitted to Eq. (9) to obtain E_{core} and r_0. Note that due to geometry optimisation, which may lead to radial displacements, the atoms in region 1 in bulk cell may not be within the same cutoff radius in the dislocated structure. Tracking atomic movement is critical to ensure E_d^{11} contains identical number of atoms in both the bulk and dislocated cells.

3. Results and discussion

3.1. Experimental observation of edge dislocation via TEM

Fig. 4 shows an TEM image of a C2S sample where the crystalline features are clearly visible via the parallel layers and the selected area electron diffraction (SAED) patterns. Moreover, there exists several defects such as edge dislocations in this image. As an example, the inset with the magnified resolution clearly demonstrates an existence of an edge dislocation in C2S. The central area encapsulated with the circle denotes the core structure of the edge dislocation. The feasibility of such a high resolution TEM imaging in cement crystals is quite exciting and can stimulate further studies such as realtime in-situ TEM imaging of edge dislocation movement and onset of plasticity under nanoindentation [58]. Note that this experimental C2S (with ~99% purity) is somewhat a mixture of all polymorphs because of the difficulty in making pure polymorphs and presence of small percentages of impurities (stabilizers) that are common additives in making different belite polymorphs stable at room temperature [60]. To understand the characteristics of the core structures in each polymorph and provide detailed information beyond the experimental observation, in what follows we focus on computational predictions and results that provide an "atomistic lens" for each polymorph.

3.2. Core structures and core displacement fields

Once the dislocated structure has been computationally introduced in the atomistic structures and minimum energy configuration is achieved, it is possible to describe the dislocation core characteristics in several ways. On the shortest scale, the bonding and atomic structure close to the core are explored. An efficient way of examining the structure of the dislocation core is plotting the displacement field of adjacent atoms along the in-plane direction. We draw arrows between the neighboring atoms before and after energy minimization with length proportional to their in-plane displacements. These movements arise from the fact that the linear elasticity is not sufficient to describe the dislocation core structure. Interestingly, some crystals undergo a dramatic rearrangement around the core while some diffuse the core distortion smoothly. Fig. 5 shows the relaxed core structures of five belite polymorphs. The atomic arrangements in Fig. 5 reveal that α_H-C2S has the most closely packed system while γ-C2S has the most space among tetrahedra. The interactions among atoms should restrict the formation of edge dislocations in α_H-C2S.

The core displacement field representation in Fig. 5 clearly demonstrates when an edge dislocation spreads onto one or more planes and allows visualization of such processes. As an example, movements around the dislocation core of α-C2S polymorph follow a clock-wise circular trend and expand outwards, indicating a core expansion during energy minimization. The core displacement fields for other four belite polymorphs are somewhat analogous. We noticed that after energy relaxation, the gap perpendicular to the slip plane caused by elastic estimation becomes smaller. This indicates that atomic interactions induced by energy minimization help towards retaining the original packing arrangement, a feature that is absent classical continuum theories of dislocations. Among all belite polymorphs, we found that γ-C2S bears the largest displacements around the core and away from the core. This is because the loosely packed structure of γ-C2S and porosity between silicon tetrahedra provides ample space to adjust final atomic

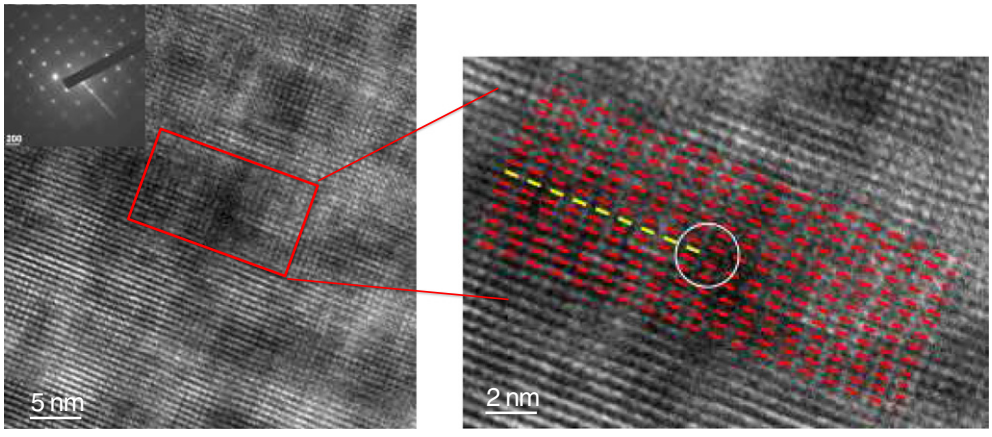

Fig. 4. A TEM image of C2S where the crystalline features are clearly visible via the parallel layers and the selected area electron diffraction (SAED) patterns. The inset demonstrates an example of an edge dislocation in C2S. The central area encapsulated with the circle denotes the core structure of the edge dislocation.

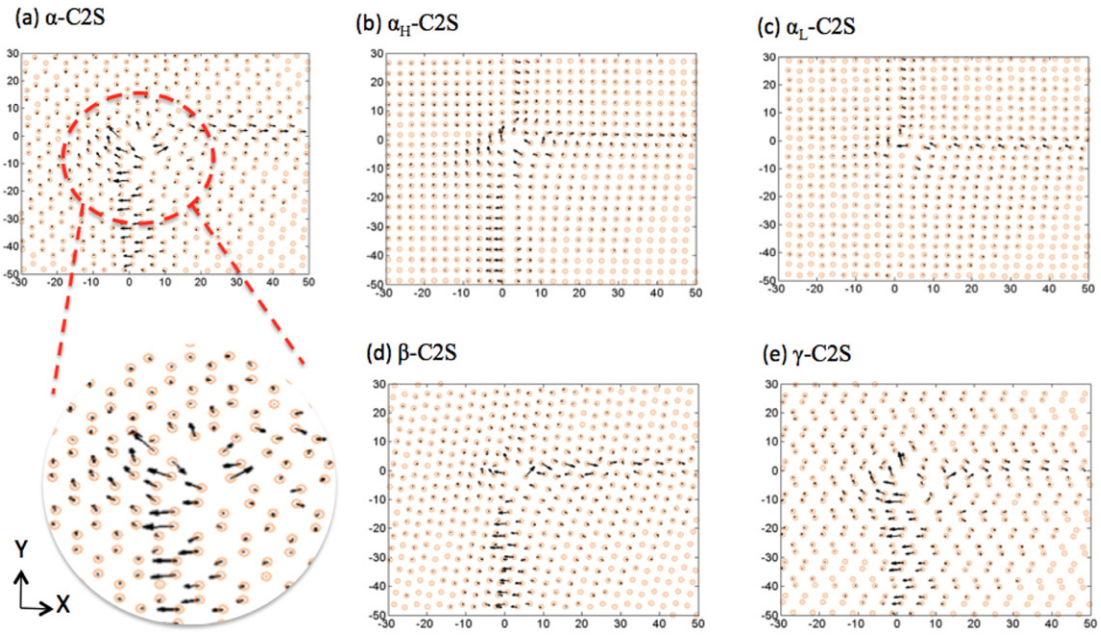

Fig. 5. (a–e) Differential displacements of α_H-C2S, α_H-C2S, α_L-C2S, β-C2S, and γ-C2S under edge dislocation. For clarity, only the positions of silicon atoms are shown with circles. Black arrows point to the movement of the silicate atoms after relaxation. For a better visualization, the length of the arrows is five times larger than the actual values. All length dimensions shown are in the Angstrom.

positions (see Fig. 2e). Simply put, the tetrahedra in γ-C2S are more independent and free to move than those of other polymorphs, which are somewhat constrained.

3.3. Dislocation core energy

Fig. 6 demonstrates the dislocation formation energy of all five belite polymorphs as a function of radius. This energy is, in general, a logarithmic function of distance (r) from the dislocation line. Clearly, α_H-C2S has the largest dislocation formation energy among all other polymorphs. This stems from the fact that any distortion in α_H-C2S involves breaking the strong Si—O bonds in its highly packed atomic arrangement. Fig. 6 and Table 2 shows the magnitudes of the core energies and core radii, which are extracted by fitting Eq. (9) to the scattered data. Strictly speaking, to compare dislocation core energies among different polymorphs, core energies must be evaluated to a common radius (as opposed to direct extraction of core energies obtained from the fit of Eq. (9), which correspond to different core radii) [59]. However, in view of Table 2, all the core radii are ~14 Å except α_H-C2S whose core radios is ~2 Å shorter than all other polymorphs. Given that the core energy of α_H-C2S is significantly larger than others, one can simply confirm via Fig. 6 that the correction of the core energy for a common radius does not change the overall picture; that is α_H-C2S still possesses the largest core energy, ~1.9 eV/Å, and γ-C2S the lowest core energy, ~0.18 eV/Å, among all belite polymorphs. To better understand the sources of this disparity, Fig. 6 shows the correlation of the Burgers vectors, Poisson's ratios and average shear moduli of all belite polymorphs obtained from the Reuss-Voigt-Hill method [60]. Considering the almost identical values of these parameters (i.e. Burgers vectors, the Poisson ratios and shear moduli) among all belite polymorphs, it seems the chief source of disparity between the core formations energies is the difference in edge dislocation core structure, i.e., the atomic arrangements around the core. As shown in Fig. 2, the atoms in α_H-C2S are highly close-packed and present a chain-like character whereas the large channels and pores in γ-C2S "take away" the torsion from the edge dislocation and allow significant flexibility between interacting tetrahedra, as manifest by large displacement field of γ-C2S around the core to freely absorb the impact of dislocation disturbance (Fig. 5e). This free, rigid-body type movement of silicon tetrahedra explains the low core formation energy in γ-C2S.

Considering other polymorphs and assuming a common radius of ~13.5 Å, while α-C2S has almost an identical Burgers vector to those of α_L-C2S and β-C2S, its core energy is ~37% and ~28% smaller than those of α_L-C2S and β-C2S, respectively. Although the larger shear modulus of α_L-C2S than α-C2S may partly justify this behavior for α_L-C2S, the smaller shear modulus of β-C2S than α-C2S cannot explain this trend. Poisson's ratios cannot elucidate this behavior either since they are all around 0.3–4 and their small alterations do not contribute significantly to the core energies. Again the core structure of these low symmetry polymorphs and their complex non-linear arrangement around the core contribute to these trends. Therefore, in spite of the common intuition based on simple crystalline materials that the larger the shear modulus, the higher the core energies, we found that this is not necessarily the case for low symmetry dicalcium silicate polymorphs due to the complicated atomic arrangement around the dislocation

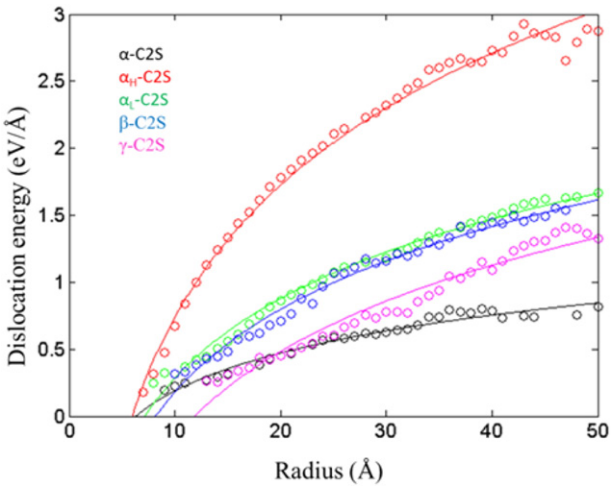

Fig. 6. Dislocation formation energies as a function of radius for five belite phases. The solid lines are the fitted curves to Eq. (9).

Table 2
Core energies and core radii of belite polymorphs.

	α-C2S	α_H-C2S	α_L-C2S	β-C2S	γ-C2S
Core energy (eV)	0.33	1.99	0.53	0.46	0.18
Core radius (Å)	14.01	11.94	13.34	13.63	14.4

core. Nevertheless, the crystals with larger core energies have generally smaller dislocation core radii (Table 2).

3.4. Impacts on crystal growth and grinding mechanisms

Here, we focus on potential influence of the core on nucleation rate and reactivity, and how the edge dislocation may impact crystal growth such as the growth of calcium-silicate-hydrate (C-S-H) phase, the key hydration product of Ca_2SiO_4 that is responsible for mechanical properties of cement pastes. It is widely known that the emergent ends of pure screw dislocations form regenerative surface steps that can promote crystal growth. Although less obvious, this effect has been observed and validated in dislocations with mixed character and pure edge dislocations as well [3–4,61]. More precisely, not only the spiral step pattern of screw dislocation, but also the closed-loop patterns arising from transverse growth steps generated at edge dislocations can influence crystal growth [4]. Such patterns in Ca2SiO4 serves as a basin for water molecules, and the hydration process might be expedited by increasing dislocation density [45].

Dislocations with smaller core energy form easier and multiply faster upon deformation [53], thereby providing more hot spots for dissociation and crystal growth. In light of Fig. 7 and considering only edge dislocation mediated crystal growth, our findings suggest the following ranking (in order) for crystal growth in belite polymorphs: γ-C2S > α-C2S > β-C2S > α_L-C2S > α_H-C2S. Given that the pure γ-C2S polymorph does not exist in real clinker due to required stabilizer such as Na_2O, Al_2O_3, K_2O, and $BaSO_4^{3-}$ (which consequently change the kinetics and energetics of edge dislocation) [62], our results indicate that indeed α-C2S has the highest reactivity among all Ca_2SiO_4 polymorphs. This is in line with previous reports on the effect of dislocation on reactivity of the belite polymorphs [63], and match extremely well with experimental evidence reporting higher reactivity of α-C2S over β-C2S when mixing with water [64]. As discussed above, the steps and topology of the dislocation core also influence the crystal growth and energetics of the major adsorbate sites, which are typically around the core geometry in dislocations terminated at a surface [65]. Hence, when searching for reaction accelerators (inhibitors) to control and modulate cement hydration, it will be suitable to find those adsorbates that bind and dissociate (block) the dislocation core sites.

Finally, we turn on attention on the knowledge of dislocation mobilities, which can provide important information on the inherent materials features such as ductility and brittleness, impacting the fracture and grinding mechanisms of cement clinkers. Since a complete dynamic analysis of dislocations is beyond the scope of the present manuscripts, as a rough estimate to assess the mobility of the dislocation, we approximate the Peierls stress, the force needed to move a dislocation, from a formula developed by Peierls and Nabarro as [1]

$$\tau_p = \frac{2\pi}{b^2} E_p = \frac{2G}{(1-\nu)} \exp\left(\frac{-2\pi w}{b}\right) \quad (11)$$

where $w = a/(1-\nu)$ is the core width as in edge dislocation where a is planar basal distance perpendicular to Burgers vector, G is the shear modulus, b is the Burgers vector, and ν is the Poisson ratio. By definition, a larger Peierls stress reveals a more brittle material, i.e. lower mobility [66], which is favorable for grinding of cement clinkers (brittle clinkers break rapidly and require less energy). Table 3 presents the approximate Peierls stresses for edge dislocations in belite polymorphs. It appears that the β-C2S has the highest Peierls stress suggesting that the

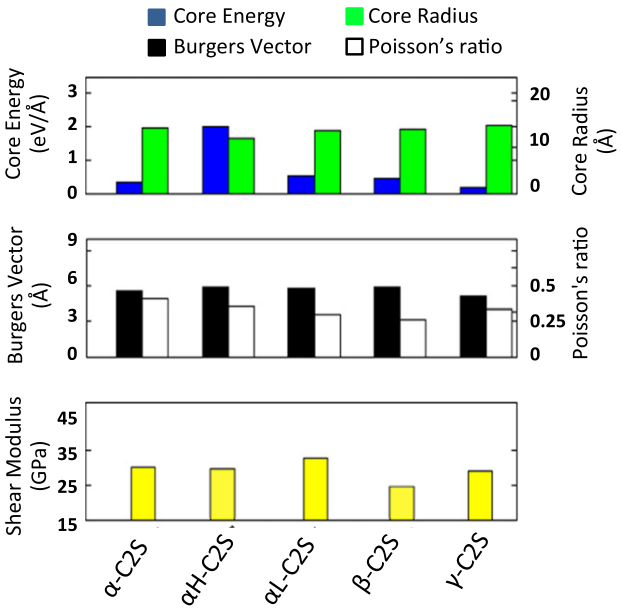

Fig. 7. Core energies, core radii, Burgers vectors, Poisson's ratios and shear moduli of belite polymorphs.

edge dislocations in β-C2S rarely move and the crystal manifest brittle characteristics. On the other hand, the high temperature belite polymorphs such as α_H-C2S and α-C2S exhibit a relatively ductile behavior. Note that this finding must not be confused with thermally activated slip processes since the brittle-to-ductile transition temperature of such rock-type materials are typically quite high (~2000 K) and even may need high confining pressure (~3000 MPa) to exhibit ductility [67].

Lastly, we remind that all above observations are solely based on pure edge dislocations. We remind that while a C2S crystal may show resistance (and thus brittleness) to the movement of edge dislocation, it may be a preferred host for the movement of screw dislocation. Therefore, it may not be surprising to realize that while β-C2S is more brittle from this edge dislocations study, α-C2S tends to be more brittle from a screw dislocation perspective [63]. Of cause, in reality a clinker may consist of various imperfections like point defects, edge and screw (mixed) dislocations and twining deformations, etc., which must be considered all together for a realistic assessment of the brittleness. Thus, future studies on mixed dislocations, twining deformations and their interactions with edge and screw dislocations are needed to provide more refined data on grinding and crystal growth processing for C2S polymorphs. Furthermore, all our atomistic modeling in this work are performed at the idealized limit of behavior at T = 0 K to exclude the effects of thermally activated processes [68–69]. Although C2S polymorphs are stable at finite temperatures, their stabilized 0 K crystals represent metastable states whose energies might be slightly larger than otherwise perfect stable structures at 0 K. This issue will not have a significant impact on key dislocation-mediated properties (e.g. core energy, structure) which are mainly based on mechanistic processes as opposed to thermally activated processes. For instance, a recent

Table 3
Estimation of Peierls stresses for edge dislocation in belite polymorphs.

Belite polymorphs	Peierls stress (MPa)
α-C2S	3.586
α_H-C2S	1.313
α_L-C2S	34.145
β-C2S	165.442
γ-C2S	2.308

work examined the effect of thermal motion on defect nucleation, and it was shown that the activation energy barriers are too far high for thermal motions to play a significant role [70]. Thus, while we expect the thermal motion to have a minimal effect on our afore-mentioned results, future studies are needed to analyze such effects systematically.

4. Conclusion

We studied the atomic-scale characteristics of edge dislocation in 5 polymorphs of dicalcium silicate, as a class of complex low symmetry oxides. While our experimental TEM tests revealed a clear high-resolution image of edge dislocation in C2S, we performed extensive computations to provide an "atomistic lens" on edge dislocation characteristics. We found that γ-C2S and α-C2S polymorphs have the lowest core formation energies and thus the most favorable polymorphs for dislocations in dicalcium silicates, mainly due to their large pore channels and nearly rigid-body type movements of atoms, which take away majority of the distortions imposed by edge dislocations. Our results suggest that α-C2S crystal is the most reactive polymorph in dislocation-mediated crystal growth, consistent with previous reports. Furthermore, we identified β-C2S as the most brittle polymorph of belite in the context of edge dislocation. These basic knowledge of brittleness may influence micro cracking, brittleness and fracture of belite, and combined with other strategies such as use of polymers, may help devise strategies to reduce the energy associated with grinding dicalcium silicate (cement) clinkers. This information, in conjunction with the predicted nucleation rate of reactivity, core structures and displacement fields, can provide new physical insights and guiding hypotheses for experimentalist to tune the cement reactivity processes as well as grinding mechanisms.

To our knowledge, this work is the first report of atomistic-scale analysis of edge dislocations in structurally complex dicalcium silicates, and can potentially open up new opportunities for further studies, such as mixed dislocation-mediated mechanisms, brittle-to-ductile transitions, and twinning deformations and their interactions with dislocations, to provide a comprehensive understanding of deformation mechanisms in cement clinkers. Broadly, the concepts, methods and strategies of this work can impact several other oxides and low symmetry crystals such as jennite [38], layered and hybrid calcium-silicate materials [71–75], as well as recently developed realistic and combinatorial models of calcium-silicate–hydrates [76–78] and microporous materials in general [79–80].

Competing financial interest

The authors declare no competing financial interest.

Acknowledgements

R.S. acknowledges the financial support by the National Science Foundation, award numbers 1235522. The supercomputer machines utilized in this work were supported in part by NIH award NCRR S10RR02950 and an IBM Shared University Research (SUR) Award in partnership with CISCO, Qlogic and Adaptive Computing, and in part by the Data Analysis and Visualization Cyber infrastructure funded by NSF under grant OCI-0959097. We thank the discussions with Dr. Sakineh Pourmoghaddam for TEM analysis.

Appendix A. Supplementary data

Force field parameters, force field predictions of lattice parameters and elastic properties, and Reuss-Voigt-Hill approach to calculate the average shear modulus for anisotropic crystals. This materials is available free of charge via the Internet at http://pubs.acs.org. Supplementary data associated with this article can be found in the online version, at http://dx.doi.org/10.1016/j.cemconres.2016.09.012.

References

[1] D. Hull, D.J. Bacon, Introduction to Dislocations, Fourth ed. Butterworth-Heinemann, Oxford, 2001.
[2] P. Smereka, Spiral crystal growth, Physica D 138 (3–4) (2000) 282–301.
[3] J.N. Sherwood, T. Shripathi, Role of dislocations in the growth of single crystals of potash alum, Faraday Discuss. 95 (0) (1993) 173–182.
[4] J.N. Sherwood, T. Shripathi, Evidence for the role of pure edge dislocations in crystal growth, J. Cryst. Growth 88 (3) (1988) 358–364.
[5] J.E. Sinclair, Improved atomistic model of a bcc dislocation core, J. Appl. Phys. 42 (13) (1971) 5321–5329.
[6] P.C. Gehlen, J.P. Hirth, R.G. Hoagland, M.F. Kanninen, A new representation of the strain field associated with the cube-edge dislocation in a model of a α-iron, J. Appl. Phys. 43 (10) (1972) 3921–3933.
[7] S. Ismail-Beigi, T.A. Arias, Ab initio study of screw dislocations in Mo and Ta: a new picture of plasticity in bcc transition metals, Phys. Rev. Lett. 84 (7) (2000) 1499–1502.
[8] L.H. Yang, P. Söderlind, J.A. Moriarty, Accurate atomistic simulation of (a/2) ⟨111⟩ screw dislocations and other defects in bcc tantalum, Philos. Mag. A 81 (5) (2001) 1355–1385.
[9] T. Kaplan, F. Liu, M. Mostoller, M.F. Chisholm, V. Milman, First-principles study of impurity segregation in edge dislocations in Si, Phys. Rev. B 61 (3) (2000) 1674–1676.
[10] F. Liu, M. Mostoller, V. Milman, M.F. Chisholm, T. Kaplan, Electronic and elastic properties of edge dislocations in Si, Phys. Rev. B 51 (23) (1995) 17192–17195.
[11] J.R.K. Bigger, D.A. McInnes, A.P. Sutton, M.C. Payne, I. Stich, R.D. King-Smith, D.M. Bird, L.J. Clarke, Atomic and electronic structures of the 90° partial dislocation in silicon, Phys. Rev. Lett. 69 (15) (1992) 2224–2227.
[12] M.I. Heggie, C.P. Ewels, N. Martsinovich, S. Scarle, R. Jones, J.P. Goss, B. Hourahine, P.R. Briddon, Glide dislocations in diamond: first-principles calculations of similarities with and differences from silicon and the effects of hydrogen, J. Phys. Condens. Matter 14 (48) (2002) 12689.
[13] N. Martsinovich, M.I. Heggie, C.P. Ewels, First-principles calculations on the structure of hydrogen aggregates in silicon and diamond, J. Phys. Condens. Matter 15 (39) (2003) S2815.
[14] J. Rabier, J. Soullard, M.P. Puls, Atomistic calculations of point-defect interactions with an edge dislocation in NiO, Philos. Mag. A 61 (1) (1990) 99–108.
[15] J. Rabier, M.P. Puls, On the core structures of edge dislocations in NaCl and MgO. Consequences for the core configurations of dislocation dipoles, Philos. Mag. A 59 (4) (1989) 821–842.
[16] M.P. Puls, M.J. Norgett, Atomistic calculation of the core structure and Peierls energy of an (a/2) [110] edge dislocation in MgO, J. Appl. Phys. 47 (2) (1976) 466–477.
[17] M.P. Puls, C.H. Woo, M.J. Norgett, Shell-model calculations of interaction energies between point defects and dislocations in ionic crystals, Philos. Mag. 36 (6) (1977) 1457–1472.
[18] M.P. Puls, Vacancy-dislocation interaction energies in MgO a re-analysis, Philos. Mag. A 47 (4) (1983) 497–513.
[19] M.P. Puls, Vacancy-dislocation interaction energies in MgO, Philos. Mag. A 41 (3) (1980) 353–368.
[20] R.G. Hoagland, J.P. Hirth, P.C. Gehlen, Atomic simulation of the dislocation core structure and Peierls stress in alkali halide, Philos. Mag. 34 (3) (1976) 413–439.
[21] G.W. Watson, E.T. Kelsey, S.C. Parker, Atomistic simulation of screw dislocations in rock salt structured materials, Philos. Mag. A 79 (3) (1999) 527–536.
[22] A.M. Walker, P. Carrez, P. Cordier, Atomic-scale models of dislocation cores in minerals: progress and prospects, Mineral. Mag. 74 (3) (2010) 381–413.
[23] S. Amelinckx, R. Gever, J.V. Landuyt, Diffraction and Imaging Techniques in Materials Science, 2nd ed., 1978 (North-Holland).
[24] P.J. Goodhew, J. Humphreys, R. Beanlan, Electron Microscopy and Analysis, third ed. Taylor & Francis, London, 2001.
[25] M.F. Chisholm, S.J. Pennycook, Direct imaging of dislocation core structures by Z-contrast STEM, Philos. Mag. 86 (29–31) (2006) 4699–4725.
[26] R.E. Peierls, On the size of a dislocation, Proc. Phys. Soc. Lond. 52 (1940).
[27] F.R.N. Nabarro, Dislocations in a simple cubic lattice, Proc. Phys. Soc. 59 (2) (1947) 256.
[28] G. Schoeck, The Peierls model: progress and limitations, Mater. Sci. Eng. A 400–401 (0) (2005) 7–17.
[29] M. Mostoller, M.F. Chisholm, T. Kaplan, New extended point defect structure in diamond cubic crystals, Phys. Rev. Lett. 72 (10) (1994) 1494–1497.
[30] E. Clouet, L. Ventelon, F. Willaime, Dislocation core energies and core fields from first principles, Phys. Rev. Lett. 102 (5) (2009).
[31] W. Cai, V.V. Bulatov, J. Chang, J. Li, S. Yip, Anisotropic elastic interactions of a periodic dislocation array, Phys. Rev. Lett. 86 (25) (2001) 5727–5730.
[32] E. Clouet, Elastic energy of a straight dislocation and contribution from core tractions, Philos. Mag. 89 (19) (2009) 1565–1584.
[33] A.M. Walker, J.D. Gale, B. Slater, K. Wright, Atomic scale modelling of the cores of dislocations in complex materials part 1: methodology, Phys. Chem. Chem. Phys. 7 (17) (2005) 3227–3234.
[34] A.M. Walker, J.D. Gale, B. Slater, K. Wright, Atomic scale modelling of the cores of dislocations in complex materials part 2: applications, Phys. Chem. Chem. Phys. 7 (17) (2005) 3235–3242.
[35] A.M. Walker, B. Slater, J.D. Gale, K. Wright, Predicting the structure of screw dislocations in nanoporous materials, Nat. Mater. 3 (10) (2004) 715–720.
[36] A. Walker, Simulation of screw dislocations in wadsleyite, Phys. Chem. Miner. 37 (5) (2010) 301–310.
[37] H.F. Taylor, Cement Chemistry, 2 ed. London, Thomas Telford Publishing, 1997.
[38] R. Shahsavari, M.J. Buehler, R.J.M. Pellenq, F.-J. Ulm, First-principles study of elastic constants and interlayer interactions of complex hydrated oxides: case study of tobermorite and jennite, J. Am. Ceram. Soc. 92 (10) (2009) 2323–2330.

[39] S.N. Ghosh, Advances in Cement Technology: Chemistry, Manufacture and Testing, Taylor & Francis, 2002.
[40] W.G. Mumme, R.J. Hill, G. Bushnell-Wye, E.R. Segnit, Rietveld crystal structure refinements, crystal chemistry and calculated powder diffraction data for the polymorphs of dicalcium silicate and related phases, Neues Jahrbuch fuer Mineralogie - Abhandlungen 169 (1995) 35–68.
[41] J. Barbier, B.G. Hyde, The structures of the polymorphs of dicalcium silicate, Ca_2SiO_4, Acta Crystallogr. B 41 (6) (1985) 383–390.
[42] X. Feng, X. Min, C. Tao, Study on the stru cture and characteristic of dicalcium silicate with quantum chemistry calculations, Cem. Concr. Res. 24 (7) (1994) 1311–1316.
[43] D.K. Smith, A. Majumdar, F. Ordway, The crystal structure of [gamma]-dicalcium silicate, Acta Crystallogr. 18 (4) (1965) 787–795.
[44] K.H. Jost, B. Ziemer, R. Seydel, Redetermination of the structure of [beta]-dicalcium silicate, Acta Crystallogr. B 33 (6) (1977) 1696–1700.
[45] P. Juilland, E. Gallucci, R. Flatt, K. Scrivener, Dissolution theory applied to the induction period in alite hydration, Cem. Concr. Res. 40 (6) (2010) 831–844.
[46] J.A.N. Skalny, J.N. Maycock, Scanning electron microscopy of industrial cement clinkers, J. Am. Ceram. Soc. 57 (6) (1974) 253–256.
[47] G.W. Groves, Portland cement clinker viewed by transmission electron microscopy, J. Mater. Sci. 16 (4) (1981) 1063–1070.
[48] K.E. Hudson, G.W. Groves, The structure of alite in Portland cement clinker - TEM evidence, Cem. Concr. Res. 12 (1) (1982) 61–68.
[49] R.T. Cygan, W.H. Casey, M.B. Boslough, H.R. Westrich, M.J. Carr, G.R. Holdren Jr., Dissolution kinetics of experimentally shocked silicate minerals, Chem. Geol. 78 (3–4) (1989) 229–244.
[50] Y.G. Wang, B.S. Zou, K.H. Kuo, X.J. Feng, L. Wang, S.Z. Long, High-resolution electron microscopy study of belite, J. Mater. Sci. 24 (3) (1989) 877–880.
[51] R. Shahsavari, L. Tao, L. Chen, Structure, energetics, and impact of screw dislocations in tricalcium silicates, J. Am. Ceram. Soc. (2016) (n/a-n/a).
[52] P.C. Hewlett, F.M. Lea, Lea's Chemistry of Cement and Concrete, Fourth edition Elsevier Butterworth-Heinemann, Oxford: UK, 1998.
[53] J.P. Hirth, J. Lothe, Theory of Dislocations, 2nd ed. John Wiley & Sons, New York, 1982 435.
[54] J.D. Gale, A.L. Rohl, The general utility lattice program (GULP), Mol. Simul. 29 (5) (2003) 291–341.
[55] R.T. Cygan, J.-J. Liang, A.G. Kalinichev, Molecular models of hydroxide, oxyhydroxide, and clay phases and the development of a general force field, J. Phys. Chem. B 108 (4) (2004) 1255–1266.
[56] R.J. Kirkpatrick, A.G. Kalinichev, J. Wang, Molecular dynamics modelling of hydrated mineral interlayers and surfaces: structure and dynamics, Mineral. Mag. 69 (3) (2005) 289–308.
[57] J. K., A. K., J. W., Molecular modeling of confined fluids and solid-fluid interfaces in portland cement and related materials, in: P. Bartos (Ed.), NanoTechnology in Construction, The Royal Society of Chemistry, United Kingdom, 2004.
[58] A.M. Minor, S.A. Syed Asif, Z. Shan, E.A. Stach, E. Cyrankowski, T.J. Wyrobek, O.L. Warren, A new view of the onset of plasticity during the nanoindentation of aluminium, Nat. Mater. 5 (9) (2006) 697–702.
[59] A.T. Blumenau, M.I. Heggie, C.J. Fall, R. Jones, T. Frauenheim, Dislocations in diamond: core structures and energies, Phys. Rev. B 65 (20) (2002) 205205.
[60] R. Hill, The elastic behaviour of a crystalline aggregate, Proc. Phys. Soc. Sect. A 65 (5) (1952) 349.
[61] E. Bauser, H. Strunk, Analysis of dislocations creating monomolecular growth steps, J. Cryst. Growth 51 (2) (1981) 362–366.
[62] I. Nettleship, K.G. Slavick, Y.J. Kim, W.M. Kriven, Phase transformations in dicalcium silicate: I, fabrication and phase stability of fine-grained β phase, J. Am. Ceram. Soc. 75 (9) (1992) 2400–2406.
[63] R. Shahsavari, L. Chen, Screw dislocations in complex, low symmetry oxides: core structures, energetics, and impact on crystal growth, ACS Appl. Mater. Interfaces 7 (4) (2015) 2223–2234.
[64] J.F. Y., Highly reactive dicalcium silicates for belite cementProceeding of the International RILEM Conference on Concrete: From Material to Structure 1988, pp. 1–15.
[65] G.W. Watson, P.M. Oliver, S.C. Parker, Atomistic simulation of crystal growth at the a ⟨1 0 0⟩ screw dislocation terminating at the {1 0 0} surface of MgO, Surf. Sci. 474 (1–3) (2001) L185–L190.
[66] S.M. Han, G. Feng, J.Y. Jung, H.J. Jung, J.R. Groves, W.D. Nix, Y. Cui, Critical-temperature/Peierls-stress dependent size effects in body centered cubic nanopillars, Appl. Phys. Lett. 102 (4) (2013).
[67] M.S. Paterson, Experimental Rock Deformation - The Brittle Field, Springer, Berlin, 2005.
[68] T. Zhu, J. Li, K.J. Van Vliet, S. Ogata, S. Yip, S. Suresh, Predictive modeling of nanoindentation-induced homogeneous dislocation nucleation in copper, J. Mech. Phys. Solids 52 (3) (2004) 691–724.
[69] T. Zhu, J. Li, Ultra-strength materials, Prog. Mater. Sci. 55 (7) (2010) 710–757.
[70] G. Xu, A.S. Argon, Energetics of homogeneous nucleation of dislocation loops under a simple shear stress in perfect crystals, Mater. Sci. Eng. A 319–321 (0) (2001) 144–147.
[71] R. Shahsavari, R.J.M. Pellenq, F.-J. Ulm, Empirical force fields for complex hydrated calcio-silicate layered materials, Phys. Chem. Chem. Phys. 13 (3) (2011) 1002–1011.
[72] N. Sakhavand, R. Shahsavari, Universal composition-structure-property maps for natural and biomimetic platelet-matrix composites and stacked heterostructures, Nat. Commun. 6 (2015) 6523.
[73] S. Jalilvand, R. Shahsavari, Molecular mechanistic origin of nanoscale contact, friction, and scratch in complex particulate systems, ACS Appl. Mater. Interfaces 7 (5) (2015) 3362–3372.
[74] N. Sakhavand, P. Muthuramalingam, R. Shahsavari, Toughness governs the rupture of the interfacial H-bond assemblies at a critical length scale in hybrid materials, Langmuir 29 (25) (2013) 8154–8163.
[75] N. Zhang, R. Shahsavari, Balancing strength and toughness of calcium-silicate-hydrate via random voids and particles inclusions, J. Mech. Phys. Solids 96 (2016) 204–222.
[76] R.J.M. Pellenq, A. Kushima, R. Shahsavari, K.J.V. Vliet, M.J. Buehler, S. Yip, F.J. Ulm, A realistic molecular model of cement hydrates, Proc. Natl. Acad. Sci. 106 (38) (2009) 16102–16107.
[77] M.J. Abdolhosseini Qomi, K.J. Krakowiak, M. Bauchy, K.L. Stewart, R. Shahsavari, D. Jagannathan, D.B. Brommer, A. Baronnet, M.J. Buehler, S. Yip, et al., Combinatorial molecular optimization of cement hydrates, Nat. Commun. 5 (2014).
[78] R. Shahsavari, Hierarchical Modeling of Structure and Mechanics of Cement Hydrate, 2011.
[79] M.A. Rafiee, T.N. Narayanan, D.P. Hashim, N. Sakhavand, R. Shahsavari, R. Vajtai, P.M. Ajayan, Hexagonal boron nitride and graphite oxide reinforced multifunctional porous cement composites, Adv. Funct. Mater. 23 (45) (2013) 5624–5630.
[80] M. Prakash, N. Sakhavand, R. Shahsavari, H_2, N_2, and CH_4 gas adsorption in zeolitic imidazolate framework-95 and -100: Ab initio based grand canonical Monte Carlo simulations, J. Phys. Chem. C 117 (46) (2013) 24407–24416.